Journal of Molecular Liquids 438 (2025) 128770

Contents lists available at ScienceDirect

Journal of Molecular Liquids

journal homepage: www.elsevier.com/locate/molliq

Molecular insights into the binding of human serum albumin to charged dendritic nanomicelles: A synergistic experimental and in silico approach

Gabriele Cavalieri [a], Domenico Marson [a], Dinesh Dhumal [b], Ling Peng [b], Erik Laurini [a,*], Sabrina Pricl [a,c]

[a] Molecular Biology and Nanotechnology Laboratory (MolBNL@UniTS), DEA, University of Trieste, Piazzale Europa 1, 34127 Trieste, Italy
[b] Aix Marseille University, CNRS, Center Interdisciplinaire de Nanoscience de Marseille, UMR 7325, 13288 Marseille, France
[c] Department of General Biophysics, Faculty of Biology and Environmental Protection, University of Lodz, ul. Pomorska 141/143, 90-236 Łódź, Poland

ARTICLE INFO

Keywords:
Isothermal titration calorimetry
Self-assembly nanomicelle
Human serum albumin
Binding interaction
Molecular dynamics simulations

ABSTRACT

Understanding the interaction between dendritic nanostructures and plasma proteins is critical for optimizing their in vivo behavior and biocompatibility. In this study, we investigate the binding of human serum albumin (HSA) to a set of amphiphilic poly(amidoamine) dendrimers, both as individual monomers and as self-assembled charged nanomicelles (**1@-A**, **1@-TA**, and **1@-COOH**). A comprehensive set of techniques, including fluorescence spectroscopy, circular dichroism, isothermal titration calorimetry, dynamic light scattering, and atomistic molecular dynamics simulations, was employed to assess binding affinity, conformational effects, and complex stoichiometry resulting from the interactions between the serum protein and the dendritic nanostructures. Isothermal titration calorimetry quantified stronger HSA binding for nanomicelles (Kd = 1.15 ± 0.64 μM for 1@-A; 4.29 ± 0.57 μM for 1@-COOH; 8.10 ± 0.11 μM for 1@-TA) relative to monomers (K_d = 112 ± 11, 89 ± 21, and 104 ± 18 μM for 1-A, 1-TA, and 1-COOH, respectively). The thermodynamic signatures differed markedly: nanomicelles exhibited favorable enthalpy (ΔH = −4.07 ± 0.05 to −6.53 ± 0.04 kcal/mol) with modest entropic contributions (−TΔS = −4.09 ± 0.40 to −0.80 ± 0.04 kcal/mol), whereas monomers were entropy-driven (ΔH = +2.88 ± 0.14 to +3.12 ± 0.10 kcal/mol; −TΔS = −8.51 ± 0.21 to −8.41 ± 0.23). Spectroscopic analyses indicated that HSA retained its secondary and tertiary structures upon interaction and confirmed the formation of stable protein–nanomicelle complexes. Computational modeling revealed distinct interaction patterns at the HSA–nanomicelle interface. Together, these findings demonstrate how the structural and surface properties of dendritic nanomicelles can modulate their interaction with proteins, offering valuable insights for future design strategies. Given that the formation of a soft protein corona, especially around micelles, plays a pivotal role in protein–nanomaterial interactions, the results presented here may constitute a key step toward the rational design of next-generation nanomedicine platforms.

1. Introduction

With the increasing incidence of hard-to-treat infections, bacterial resistance to antibiotics has become a major global health concern [1]. In this context, the development of novel antibacterial agents is imperative. Amphiphilic antibacterial detergents and compounds that mimic naturally occurring antimicrobial peptides represent particularly promising candidates. Among these, poly(amidoamine) (PAMAM) dendrimers have attracted considerable interest due to their exceptional biocompatibility - conferred by their peptide-mimetic nature due to peptide mimicry, and their resistance to enzymatic degradation, which is afforded by their dendritic architecture. In addition, they can be easily obtained through robust synthetic protocols and commercial sources. Building on our previous work, we have shown that amphiphilic dendrimers (AD) composed of a small hydrophilic PAMAM dendron bearing a charged terminal group – such as primary amine, tertiary amine, carboxylate, or guanidinium - and a long hydrophobic alkyl tail exhibit potent antibacterial action [2,3]. Notably, the amine-terminated dendrimer demonstrated a broad spectrum of antibacterial activity against drug-resistant strains including both Gram-positive and Gram-negative bacteria, as well as in biofilm eradication [2,3], whereas the tertiary amine-terminated dendrimer exhibited a selective antibacterial activity

* Corresponding author.
E-mail address: erik.laurini@dia.units.it (E. Laurini).

https://doi.org/10.1016/j.molliq.2025.128770
Received 21 August 2025; Received in revised form 17 October 2025; Accepted 20 October 2025
Available online 24 October 2025

against certain drug-resistant Gram-negative bacteria, and the carboxylate- and guanidine-terminated dendrimers had no notable antibacterial activity. In addition, the antibacterial activity of both tertiary amine- and amine-terminated amphiphilic dendrimers was validated in animal models of various bacterial infections [3,4].

Considering the potential for future translation of these ADs, particular attention has been devoted to investigating their interactions with serum proteins and the resulting protein corona, with a focus on one of the most abundant components, human serum albumin (HSA). Upon exposure to biological environments, nanoscale materials spontaneously acquire a protein corona on their surface, which can alter their physiochemical properties and, consequently, their interactions with biological systems, biodistribution and toxicity etc. [5]. The effects of proteins adsorption onto nanomaterials can vary substantially in terms of structural and biological responses, as reflected by the diverse pathways and compositions of the resulting coronas. In the context of therapeutic nanomedicine, such variability poses a significant challenge, as unpredictable profiles can critically influence key outcomes including nanostructure (NS) function, cellular uptake, biodistribution, immune responses, and toxicity [5]. The composition and behavior of the protein corona are closely linked to the physicochemical properties of nanomaterials and the complexity of the surrounding biological matrices. Numerous factors influence the nature and abundance of proteins adsorbed onto NSs, including size, surface charge, hydrophobicity, rigidity, and the specific biological milieu. Protein coronas are generally classified into two main types - soft and hard -, based the strength and dynamics of protein binding [5,6]. The soft corona consists of loosely bound proteins that interact reversibly and dynamically with the NS surface [5,6]. In contrast, the hard corona is composed of proteins more firmly and persistently adsorbed onto the nanomaterials, forming a more stable, tightly bound layer [5,6]. Discriminating between soft and hard protein corona formation is essential for the rational design and development of NSs intended for biomedical applications. Actually, the protein corona may act as a protective barrier, modulating the interface between a nanomaterial and its biological environment. This duality may eventually lead to opposite outcomes: on one hand, the protein corona may shield the NS from, e.g., enzymatic degradation and improving target affinity, thereby enhancing biological performance. On the other hand, however, it might sequester the NS and hinder effective interactions with the intended target [5,6].

As a first step, in this study we focused on the formation of the protein corona by HSA, the most abundant protein in human plasma. Owing to its high concentration in the bloodstream, HSA plays a pivotal role in the pharmacokinetics of many drugs, influencing their efficacy, delivery rate, biodistribution, and toxicity profiles [7]. In this context, we investigated the binding behavior of HSA with a set of structurally related amphiphilic dendrons, examined in both their monomeric and self-assembled nanomicellar forms. Specifically, we explored and characterized the interactions between HSA and three ADs bearing either positively charged head groups, i.e., primary (**1-A**) or tertiary (**1-TA**) amines, or a negatively charged group (carboxylic acid **1-COOH**) (Fig. 1). Both primary (**1-A**) or tertiary (**1-TA**) amine-terminated

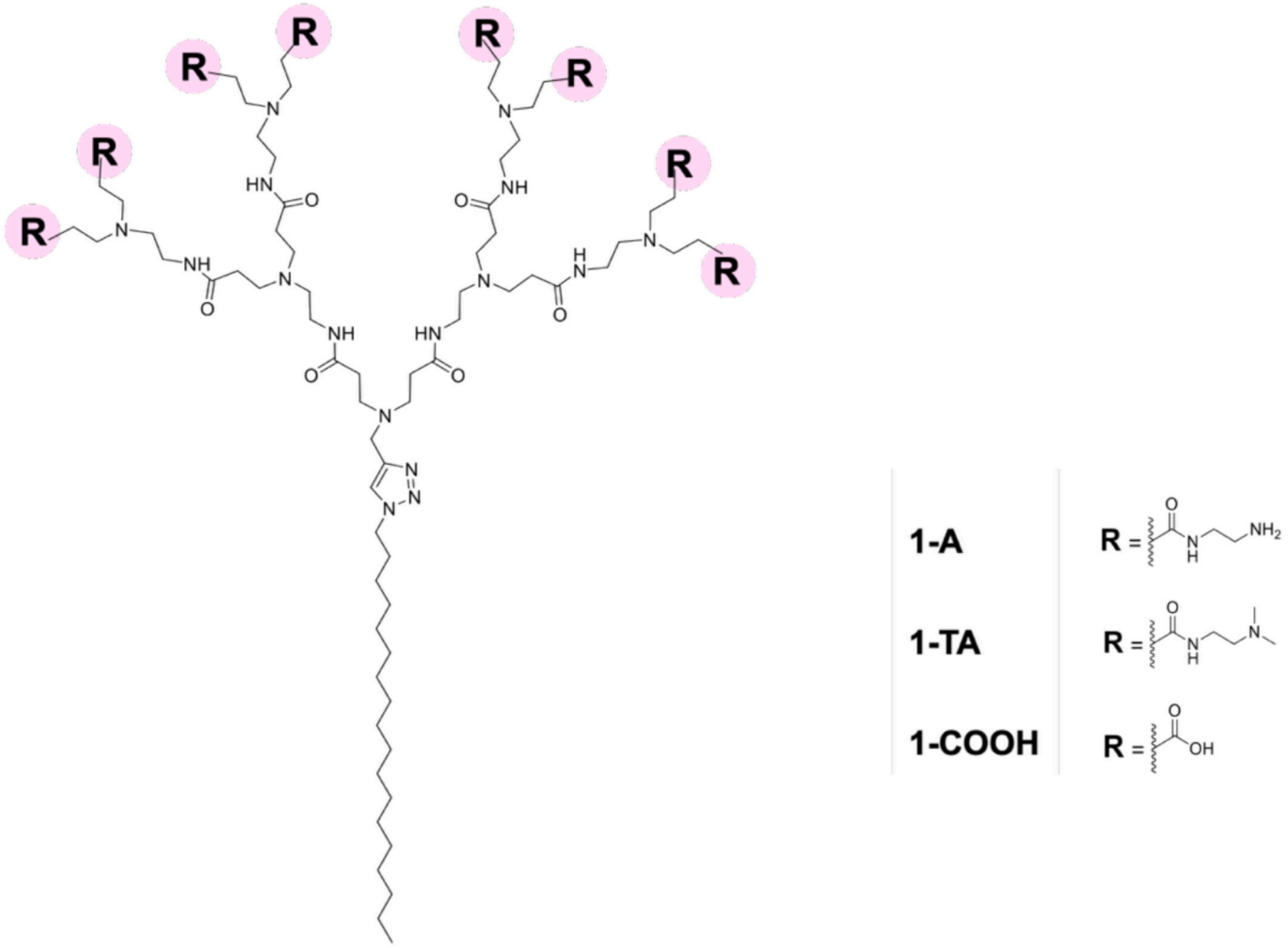

Fig. 1. Chemical structures of AD-PAMAM dendrimers **1-A**, **1-TA** and **1-COOH** bearing different terminal groups.

dendrimers have previously shown good performance as drug delivery nanovectors [8–11] as well as promising antibacterial activity [2–4]. To this end, we combined multiple experimental techniques including fluorescence spectroscopy (FS), isothermal titration calorimetry (ITC), circular dichroism (CD) spectroscopy and dynamic light scattering (DLS), with atomistic molecular dynamics (MD) simulations to (i) quantify binding affinities and elucidate thermodynamic driving forces, (ii) identify interaction hotspots, and (iii) assess structural and conformational changes upon complex formation. This integrated approach offers valuable insight into the mechanisms of dendrimer–protein recognition and supports the rational design of next generation nanocarriers with enhanced biological performance.

2. Materials and methods

2.1. Reagents and chemicals

Globulin and fatty acid-free HSA (A1887) was purchased from Signa Aldrich Inc. (Saint Louis, MO, USA). The dendrimers **1-A**, **1-TA**, and **1-COOH** were synthesized according to previously reported procedures [2,12]. All other reagents and solvents used (analytical grade) were also obtained from Sigma Aldrich.

2.2. Sample preparation and analytical procedures

A stock solution of HSA was prepared by dissolving an appropriate amount of protein in phosphate-buffered saline 1× (PBS, pH = 7.4). The protein concentration was determined by UV spectroscopy using a molar extinction coefficient (ε) value of 35,700 M^{-1} cm^{-1} at a wavelength (λ) of 280 nm [13,14]. Stock solutions of the **1-A**, **1-TA**, and **1-COOH** dendrimers were prepared in PBS buffer at final concentration of 2.0 mM.

2.3. Steady-state fluorescence spectroscopy and three-dimensional fluorescence spectroscopy

All steady-state fluorescence spectroscopy (SSFS) measurements were carried using a FP-8350 spectrofluorometer (Jasco, Japan) equipped with a thermostatic cell holder and a 1 cm pathlength quartz cuvette. The excitation wavelength (λ_{exc}) was set at 280 nm and emission spectra were recorded in the 300–400 nm range at three temperatures (298 K, 304 K, and 310 K), using 5 nm excitation and 10 nm emission bandwidths. For fluorescence quenching titrations, the HSA concentration was kept constant at 2.0 μM, while the concentrations of dendrimers (**1-A**, **1-TA**, and **1-COOH**) and their nanomicellar forms (**1@-A**, **1@-TA**, and **1@-COOH**) were varied according to their respective critical micellar concentrations (CMCs; see Figure captions for specific values). Each sample was incubated for 2 h at the target temperature prior to the acquisition of the corresponding fluorescence spectra. All FS data were corrected for inner filter effects according to the following Equation. [15]:

$$F_{corr} = F_{obs} \times 10^{(A_{exc}+A_{em})/2} \quad (1)$$

in which F_{corr} and F_{obs} represent the corrected and observed fluorescence intensities, respectively, while A_{exc} and A_{em} are the absorbances of the sample at the excitation (280 nm) and the emission (343 nm) wavelengths, respectively. The resulting inner-filter correction was modest in all cases (<10 %), with monomeric datasets typically <3 % and micellar datasets ≤8 %. Three-dimensional fluorescent spectroscopy (3D-FS) spectra were acquired under the same conditions described above by scanning λ_{exc} from 220 to 350 nm and recording emission spectra in the 220–500 nm range at 298 K. To validate the computational docking predictions for HSA/monomer systems, competitive assays were performed using Warfarin (canonical Sudlow's site I / FA7 marker) and stearic acid (fatty-acid site marker consistent with FA pockets, including FA5). Fluorescence quenching data were collected as described above. Briefly, HSA (2 μM) was pre-incubated with either warfarin (2 μM) or stearic acid (2 μM) under the same settings used in the main quenching experiments; monomer solutions were then added stepwise and emission spectra recorded.

All fluorescence spectroscopy experiments were performed in triplicate (n = 3). Reported values are mean ± Standard Deviation (SD) across the three independent repetitions.

2.4. Ultraviolet–visible (UV–Vis) spectroscopy

UV–Vis absorption spectra were recorded on a Jasco (Japan) V-730 spectrophotometer at 298 K, using quartz cuvettes (1 cm pathlength). Spectra were acquired under the same buffer and concentration conditions used for fluorescence assays. Spectra were collected over 240–400 nm and the experiments were carried out in triplicate (n = 3).

2.5. Isothermal titration calorimetry studies

The thermodynamics of HSA-dendrimer complex formation was investigated by isothermal titration calorimetry (ITC) using a MicroCal PEAQ-ITC calorimeter (Malvern, UK) at 298 K (cell volume = 208 μL). Two types of titration experiments were performed, corresponding to the monomeric and micellar forms of the amphiphilic dendrimers. In the first series of experiments, the interaction between monomeric dendrimers and HSA was studied under dilute conditions to ensure concentrations remained below the CMC. For **1-A** and **1-TA** systems, the sample cell was filled with a 5 μM PBS solution of dendrimer, and the syringe was loaded with a 50 μM PBS solution of HSA. For **1-COOH**, the dendrimer and protein concentrations were reduced to 2.5 μM and 25 μM, respectively. Each titration consisted of 12 sequential injections of 3 μL of HSA into the dendrimer-containing cell, under constant stirring at 600 rpm.

In the second set of experiments, HSA was titrated with dendrimeric micelles at concentrations well above the CMC as described in our previous works [16,17]. The sample cell contained a PBS solution of HSA at 30 μM, and the injection syringe was filled with a 900 μM solution of each AD system. A total of 18 injections (2.0 μL) were carried out under identical stirring conditions (600 rpm). To determine the concentration of micellized AD in the sample cell during titration, the total dendrimer concentration ($[AD_{tot}]$) was expressed as the sum of free monomers ($[AD_{mon}]$) and micelles ($[AD_{mic}]$), according to the following relation employing the mass conservation principle [18,19]:

$$[AD_{tot}] = [AD_{mon}] + N_{agg} \times [AD_{mic}] \quad (2)$$

where N_{agg} is the micellar aggregation number. This approach allowed accurate modeling of the titration curves, which were analyzed using a "one set of sites" binding model. The resulting fits were plotted as thermograms, providing key thermodynamic parameters including binding constant (K_d), enthalpy (ΔH) and entropy (-TΔS) change, and Gibbs free energy (ΔG).

Control experiments (not shown) were conducted to account for unspecific heats, which were subtracted from the experimental datasets to yield the corrected integrated heat values. All measurements were carried out in triplicate and results are presented as mean ± SD. Data acquisition and analysis were performed using GraphPad Prism 10.2.3 for Mac (GraphPad Software, San Diego, California USA, www.graphpad.com).

2.6. Far-UV circular dichroism spectroscopy

Far-UV circular dichroism (CD) spectra were recorded in the 200–260 nm range at 298 K using a J-1500 spectropolarimeter (Jasco, Japan) equipped with a thermostated cell holder and a PML-534 FDCD detector. Measurements were carried out at a scan rate of 20 nm min^{-1}

with a pathlength of 0.2 cm, a step size of 0.5 nm, and a bandwidth of 1 nm. Spectra were baseline-corrected using the corresponding pure buffer spectrum, and each final CD trace represents the average of three accumulations. Data were visualized and analyzed using the Jasco Spectra Manager software. The secondary structure content of HSA, both in the absence and presence of dendrimers (at 2.0 μM, below their CMC) and their nanomicellar systems (at 50 μM), was calculated from the mean residue ellipticity (MRE) values at 208 nm using the following equation:

$$MRE_{208} = \frac{\text{observed CD (mdeg)}}{10 \times C_p \times n \times l} \quad (3)$$

$$\alpha - \text{helix}\ (\%) = \left[\frac{(-MRE_{208} - 4000}{(33000 - 4000}\right] \times 100 \quad (4)$$

in which MRE_{208} is the mean residue ellipticity at $\lambda = 208$ nm (expressed in deg. cm^2 $dmol^{-1}$), C_p is the molar concentration of HSA (2.0 μM), n is the number of amino acid residues in the protein primary sequence (585), and l is the pathlength of the CD cuvette (0.2 cm). The constants while 33,000 and 4000 (deg cm^2 $dmol^{-1}$) represent the characteristic MRE_{208} values of a fully α-helical and a β-sheet/random coil structure, respectively. CD spectra were obtained in triplicate ($n = 3$) and the relevant data are reported as mean ± SD.

2.7. Dynamic light scattering and zeta potential measurements

Measurements of nanomicelle hydrodynamic diameter and zeta (ζ)-potential were carried out by dynamic light scattering (DLS) on a Zetasizer Nano-ZS (Malvern, U.K.) at 298 K. Amphiphilic dendrimers and HSA were dissolved in PBS, and measurements were performed using a 5.0 mV He—Ne laser ($\lambda = 633$ nm) at a backscattering angle θ of 173°.

2.8. Computational details

The structural characterization of the monomeric forms of the dendrimers and the self-assembly of the corresponding nanomicelles were carried out following the established protocol described in our previous studies [2,3,17,20]. The initial configuration of each HSA–AD monomer complexes was guided by structural and electrostatic considerations. In particular, each monomer features a long hydrophobic C_{18} tail, mimicking the architecture of natural fatty acids (FAs), and a polar head group bearing distinct electrostatic signatures. Binding site selection was informed by canonical FA-binding regions in HSA [21], further refined using electrostatic potential maps computed with Delphi 8.5 (**Fig. S1**) [17,22]. Molecular docking was performed with AutoDock Vina [23], restricting the search space to selected FA pockets. The top-scoring pose for each monomer was used to initialize MD simulations. Atomistic models of the HSA/nanomicelle complexes were constructed based on electrostatic surface potential analysis of the protein. Although HSA is mildly acidic overall, its surface charge distribution is highly heterogeneous, with distinct patches of positive and negative potential. A large contiguous anionic region, involving domains IA, IIA, and IIB, was identified (**Fig. S1**, left panel) and selected as the interaction site for the cationic nanomicelles **1@-A** and **1@-TA**. Based on the ITC and the DLS results, four HSA molecules were arranged around the nanomicelle to interface with this negatively charged region. A comparably extended cationic region is not evident on the protein surface. However, a positively charged area becomes accessible upon reorientation of HSA to expose subdomains IB, IIB, and IIIB (Fig. S1, right panel). This configuration was used to model the complex with the anionic nanomicelle **1@-COOH**, positioning three HSA molecules near the carboxylate-terminated dendrimer surface, according to the experimental evidence. All systems were energy-minimized and equilibrated prior to production MD runs. Atom types were assigned according to the GAFF2 force field [24], and partial atomic charges were derived using the RESP method via the RED server [25]. The crystal structure of HSA was retrieved from the Protein Data Bank (PDB ID: 4K2C) [26] and parameterized using the AMBER ff14SB force field [27]. To compute the electrostatic potential distribution around the HSA surface - required for proper positioning of the protein with respect to the charged nanomicelles - we employed the Delphi v8.5 program [22], using the following parameters: internal dielectric constant = 4, SCALE = 2.0, PERFIL = 70.0, and ionic strength = 0.15 M. Similar parameters were adopted to estimate the zeta potential, with explicit ions included and the SURFPOT parameter set to 4.0 Å [28].

All systems (monomers, nanomicelles, HSA, and their complexes) were solvated in a box of TIP3P water molecules [29], extending at least 15 Å beyond the solute in all directions. Sodium and chloride ions were added to achieve a physiological ionic strength of 0.15 M. Full simulation protocols are detailed in our earlier work [2,17,20]. Briefly, each system underwent energy minimization, followed by staged equilibration: (i) gradual heating to 298 K and 1.0 atm, and (ii) progressive release of positional restraints on solute heavy atoms. Subsequently, 1.0 μs of unrestrained molecular dynamics (MD) simulations were performed in the NPT ensemble. Unless otherwise specified, data for structural and energetic analyses were collected from the final 100 ns of each trajectory, during which all systems had reached a stable state. Binding free energy calculations were performed using the MM/GBSA method [30] as implemented in the MMPBSA.py module of AmberTools [31], with the internal dielectric constant set to 16 to account for the highly charged interface environment. Structural analyses were conducted using CPPTRAJ [32] (AMBER22) and custom in-house Python scripts. All simulations were performed using AMBER 22 [33] on our local hybrid GPU/CPU cluster and on the Marconi-100 high-performance computing system (CINECA, Italy).

3. Results

3.1. Analysis of fluorescence quenching

Intrinsic fluorescence spectroscopy of HSA – dominated by its single tryptophan residue (Trp214) - is a well-established tool for investigating conformational changes and protein-ligand interactions [34]. In this study, fluorescence quenching experiments were employed to assess the binding interactions between HSA and both monomeric and nanomicellar forms of the ADs. However, the quantitative interpretation of quenching data, particularly in terms of binding constants (e.g., K_a or n) has been increasingly questioned. In particular, van de Weert and colleagues [35] critically noted that the underlying assumptions of Stern–Volmer-based analysis are frequently violated in complex systems like HSA/drug ensembles. This is particularly relevant when ligands exhibit heterogeneous binding modes, induce local environmental perturbations near the fluorophore, or promote protein conformation changes upon association. As a result, affinity constants derived from fluorescence data differ significantly from thermodynamic measurements and can even be misleading when interpreted mechanistically.

In light of these considerations, fluorescence data in this study were not used to extract thermodynamic binding parameters. Instead, fluorescence quenching was employed qualitatively and semi-quantitatively to confirm the occurrence of binding events and to compare the relative quenching efficiency among the various AD derivatives. The Stern-Volmer constant (K_{SV}), obtained by linear fitting of the fluorescence intensity ratio (F_0/F) versus quencher concentration, is used here as an empirical indicator of interaction strength, enabling a comparative ranking of the systems. These findings are subsequently interpreted alongside calorimetric data, which offer a more rigorous thermodynamic characterization.

Accordingly, changes in the intrinsic fluorescence intensity of HSA were monitored upon addition of **1-A**, **1-TA**, and **1-COOH** at concentrations both below and above their respective CMCs. The corresponding

results are showed in Fig. 2 and **Fig. S2**. A gradual decrease in fluorescence intensity was observed with increasing concentrations of both the monomeric and nanomicellar forms of each amphiphilic system, consistent with binding interactions between the ADs and HSA.

Fluorescence quenching may arise from a variety of mechanisms, including dynamic quenching (via molecular collisions), static quenching (via complex formation), energy transfer, or conformational changes in the protein [36]. As such, the observed quenching of HSA fluorescence by the different amphiphilic systems provides valuable insights into the nature of the binding events. The extent of quenching can be quantitatively described using the Stern-Volmer Eq. [15]:

$$\frac{F_0}{F} = 1 + K_{SV}[AD] \quad (5)$$

where F_0 is the intrinsic fluorescence intensity of HSA in the absence of quencher, F is the protein fluorescence intensity in presence of a given concentration of the quencher, K_{SV} is the Stern-Volmer quenching constant, and [AD] is the concentration of the amphiphilic dendrimer.

For each amphiphilic derivative, two Stern–Volmer constants (K_{SV}) are reported in Table 1: one for the monomeric state (**1-A/1-TA/1-COOH**) and one for the nanomicellar state (**1@-A/1@-TA/1@-COOH**), reflecting the different physical organizations of the analytes. The calculated K_{SV} values indicate that the three monomeric amphiphilic dendrimers induce only modest quenching of HSA intrinsic fluorescence, with values in the range of (1.5–1.8) $\times$ 10^4 M^{-1}. This relatively low quenching efficiency suggests that the monomeric species interact weakly with HSA, likely establishing limited physical contacts and inducing minimal perturbations to the protein structure. In such conditions, only subtle conformational changes are expected, resulting in minor alterations to the local environment surrounding Trp214 and thus a relatively small decrease in fluorescence intensity. In contrast, a marked increase in fluorescence quenching is observed for the nanomicellar systems (Fig. 2 and Table 1), with K_{SV} values reaching approximately 3.7–4.0 $\times$ 10^4 M^{-1}. This enhancement can be attributed to the multivalent nature of nanomicellar aggregates, which may offer larger space and/or simultaneously engage multiple interaction sites on the HSA surface and/or induce more extensive structural rearrangements. Furthermore, the higher local density of terminal functional groups at the nanomicelle surface likely promotes more sustained interactions with regions in close proximity to Trp214, thereby amplifying the quenching effect.

Table 1
Stern-Volmer constants (K_{SV}) for HSA fluorescence quenching in the presence of different AD-PAMAM derivatives at 298 K. Reported values represent the mean ± standard deviation from three independent experiments.

Monomeric state	HSA/1-A	HSA/1-TA	HSA/1-COOH
K_{SV} [10^4 M^{-1}]	1.61 ± 0.23	1.82 ± 0.15	1.52 ± 0.31
Micellar state	HSA/1@-A	HSA/1@-TA	HSA/1@-COOH
K_{SV} [10^4 M^{-1}]	4.01 ± 0.27	3.88 ± 0.39	3.76 ± 0.33

UV–Vis measurements were acquired under the same conditions as the fluorescence experiments to corroborate the quenching observations. For the monomeric systems, spectra closely matched that of HSA with no appreciable spectral changes, consistent with weak ground-state contacts. In contrast, the nanomicellar systems exhibited a reproducible increase of the HSA band around 280 nm (**Fig. S3**), consistent with modest-to-moderate ground-state contacts at the protein–micelle interface. This qualitative contrast mirrors the fluorescence results, where K_{SV} values are comparatively lower for monomers and higher for micelles, aligning with a scenario in which ground-state interactions are minimal for monomers and appreciable for micelles.

Moreover, Temperature-dependent fluorescence quenching was evaluated at 304 K and 310 K (**Table S1**). For the monomeric forms, K_{SV} increased with temperature, a trend consistent with entropically favored association in line with prior reports on protein–ligand and protein–nanomaterial systems where higher T promotes hydrophobic desolvation and configurational sampling [37,38]. Conversely, for the nanomicellar forms K_{SV} decreased with temperature, a behavior consistent with enthalpically driven association in which complex formation becomes less favored as T increases, in agreement with prior observations on protein binding to multivalent/clustered ligands and soft coronas reported in the literature [17].

Although, as previously discussed, fluorescence quenching might not yield reliable quantitative binding constants in complex environments, the observed differences in K_{SV} among the tested systems still offer

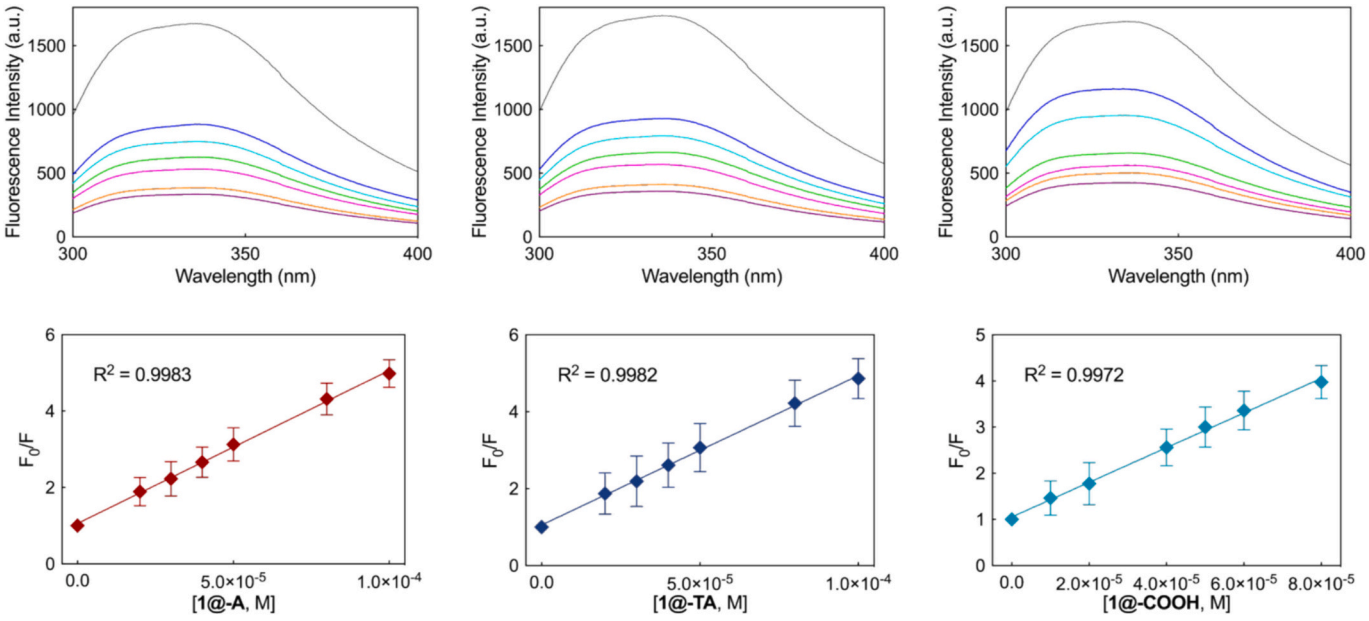

Fig. 2. (Top panels) Fluorescence emission spectra of HSA (2.0 μM) in the presence of increasing concentrations of **1@-A** (left), **1@-TA** (center), and **1@-COOH** (right) nanomicelles. Spectra include free HSA and HSA incubated with nanomicelles at the following concentrations: 20, 30, 40, 50, 80 and 100 μM for **1@-A** and **1@-TA**, and 10, 20, 40, 50, 60 and 80 μM for **1@-COOH**. (Bottom panels) Stern-Volmer plot depicting the fluorescence quenching of HSA induced by the three AD nanomicelles. Data are shown as mean ± SD (n = 3).

meaningful qualitative insight into their interaction strength. These findings support the notion that self-assembled aggregates interact more extensively with HSA than their monomeric counterparts - a hypothesis that will be further examined through ITC in the next section. Within its qualitative scope, the Stern-Volmer analysis thus provides valuable preliminary insight into the binding behavior of amphiphilic AD-PAMAM derivatives toward HSA, confirming the occurrence of interactions and highlighting differences in interaction propensity among formulations.

3.2. Binding of monomeric and nanomicellar ADs to HSA assessed using isothermal titration calorimetry

Understanding the formation of a protein corona formation is essential for predicting the behavior of nanostructures in biological environments. Isothermal Titration Calorimetry (ITC) offers a powerful approach to probe the thermodynamics of protein-nanomaterial interactions, providing direct insight into the molecular driving forces involved [39,40]. By measuring the heat exchanged upon binding in solution, ITC yields key thermodynamic parameters - including enthalpy (ΔH), entropy (ΔS), and dissociation constant (K_d) - thereby elucidating both the strength and nature of the interaction [40,41]. To quantitatively characterize the interaction between HSA and ADs, ITC experiments were performed under physiological conditions (pH 7.4). The resulting thermodynamic profiles reveal the affinity and driving forces for each system, highlighting differences between monomeric and nanomicellar forms. The corresponding data are summarized in Table 2, in Fig. 3 **and Fig. S4**.

For the monomeric forms (**1-A**, **1-TA**, and **1-COOH**), the binding thermodynamics indicate spontaneous interaction with HSA, as reflected by negative Gibbs free energy values (ΔG). All three amphiphiles exhibit dissociation constants in the mid-micromolar range (89–112 μM), along with positive enthalpy changes (ΔH = +2.88 ± 0.14 to +3.12 ± 0.10 kcal/mol). This endothermic signature, combined with strongly favorable entropy contributions (-TΔS = −8.41 ± 0.23 to −8.51 ± 0.21 kcal/mol), suggests that binding is predominantly entropy-driven. Such thermodynamic behavior is characteristic of interactions mediated by hydrophobic effects, where apolar groups insert into hydrophobic pockets of the protein, displacing structured water molecules. In these systems, the gain in entropy from desolvation and conformational freedom offsets the enthalpic penalty, overall resulting in favorable free energy of binding. In contrast, the nanomicellar systems (**1@-A**, **1@-TA**, and **1@-COOH**) display a markedly different thermodynamic profile. Titration curves for these self-assembled aggregates show clear exothermicity, with negative enthalpy values ranging from −4.07 ± 0.05 to −6.53 ± 0.04 kcal/mol. The magnitude of the enthalpic contribution increases from **1@-A** to **1@-COOH**, suggesting progressively stronger non-covalent interactions between the nanomicelle terminal groups and the protein surface. Concurrently, the entropy contributions (–TΔS) become less favorable (from −4.09 ± 0.40 kcal/mol for **1@-A** to −0.80 ± 0.04 kcal/mol for **1@-COOH**), likely reflecting entropic penalties associated with interfacial water ordering or conformational constraints upon complex formation. Nevertheless, the resulting free energy values (ΔG = −6.95 ± 0.01 to −8.16 ± 0.35 kcal/mol) confirm spontaneous binding, with significantly enhanced affinity compared to the monomeric forms (K_d = 1.15–8.10 μM). Overall, the ITC data reveal that the binding mechanism is strongly influenced by the aggregation state of the ADs. Monomeric interactions are entropy-driven and dominated by hydrophobic desolvation, whereas nanomicelle binding is primarily enthalpy-driven, involving electrostatic interactions, hydrogen bonding, and milder entropic contributions. This shift is consistent with the supramolecular organization of the nanomicelles, where peripheral charged groups are solvent-exposed and available for interaction with complementary sites on the HSA surface. Additional contributions likely arise from weak hydrophobic contacts and interfacial water rearrangement. The clear transition from entropy- to enthalpy-driven binding upon micellization highlights the impact of nanoscale self-assembly on protein recognition, with important implications for the design of functional nanocarriers.

Table 2
Thermodynamic parameters of HSA interactions with monomeric and nanomicellar AD-PAMAM derivatives obtained by ITC at 298 K.

	HSA/1-A	HSA/1-TA	HSA/1-COOH
K_d [μM]	112 ± 11	89 ± 21	104 ± 18
ΔH [kcal/mol]	3.12 ± 0.10	2.88 ± 0.14	3.03 ± 0.07
−TΔS [kcal/mol]	−8.51 ± 0.21	−8.41 ± 0.23	−8.46 ± 0.25
ΔS [kcal/mol K]	28.5 ± 0.7	28.2 ± 0.8	28.4 ± 0.8
ΔG [kcal/mol]	−5.39 ± 0.27	−5.52 ± 0.31	−5.43 ± 0.32
	HSA/1@-A	HSA/1@-TA	HSA/1@-COOH
K_d [μM]	1.15 ± 0.64	8.10 ± 0.11	4.29 ± 0.57
ΔH [kcal/mol]	−4.07 ± 0.05	−4.45 ± 0.07	−6.53 ± 0.04
−TΔS [kcal/mol]	−4.09 ± 0.40	−2.50 ± 0.08	−0.80 ± 0.04
ΔS [kcal/mol K]	13.7 ± 1.3	8.4 ± 0.3	2.7 ± 0.1
ΔG [kcal/mol]	−8.16 ± 0.35	−6.95 ± 0.01	−7.33 ± 0.08

3.3. Structural and thermal perturbation of HSA upon nanomicelle binding

3.3.1. Determination of the HSA secondary structure and thermal stability by circular dichroism spectroscopy

Circular dichroism (CD) spectroscopy is a well-established technique for probing protein secondary structures and monitoring conformational upon interaction with small molecules [42]. In this study, far-UV CD measurements were performed to assess possible structural alterations in HSA upon interaction with the amphiphilic dendrimers. The CD spectrum of native HSA exhibited the characteristic negative ellipticity bands at 208 and 222 nm, consistent with a predominantly α-helical secondary structure (Fig. 4 and Table 3).

Deconvolution of the CD spectra confirmed an α-helical content of approximately 62.6 % for native HSA, in good agreement with literature values [17,43]. Upon addition of the monomeric forms of the dendrimers no significant changes in secondary structure were observed. The α-helix content remained essentially unchanged, ranging from 62.8 % to 63.4 %, indicating that these compounds do not appreciably perturb the native conformation of the protein. A similar trend was observed for the nanomicellar forms. Slight increases in α-helix content were noted for **1@-A** (63.6 %) and **1@-TA** (63.9 %), while **1@-COOH** induced a negligible decrease (62.5 %). Overall, these results suggest that neither the monomeric nor the self-assembled forms of the three dendrimers promote significant structural destabilization or unfolding of HSA. Thermal denaturation experiments were performed by monitoring ellipticity at 222 nm over a temperature range of 298–393 K, in order to determine the melting temperature (T_m) of HSA in the presence of the various dendrimers. Native HSA exhibited a T_m of 338.30 K. Upon addition of both monomeric and nanomicellar AD-PAMAM derivatives, only minor shifts in T_m were observed, generally within ±1 K. The most pronounced decrease was recorded for **1-TA**, lowering T_m to 336.52 K. Conversely, **1@-COOH** slightly increased protein stability, with a T_m of 338.46 ± 0.31 K. These results indicate that both monomeric and self-assembled ADs exert minimal impact on the thermal stability of HSA, supporting the formation of stable protein–dendrimer complexes without significant disruption of the native protein fold.

3.3.2. Conformation stability through three-dimensional fluorescence spectroscopy

Three-dimensional fluorescence spectroscopy (3D-FS) is a sensitive technique for detecting subtle changes in the local environment of aromatic residues, particularly tryptophan, providing insights into protein conformational stability. This approach enables simultaneous acquisition of excitation-emission matrices while distinguishing intrinsic fluorescence from light scattering phenomena, and is widely used to study

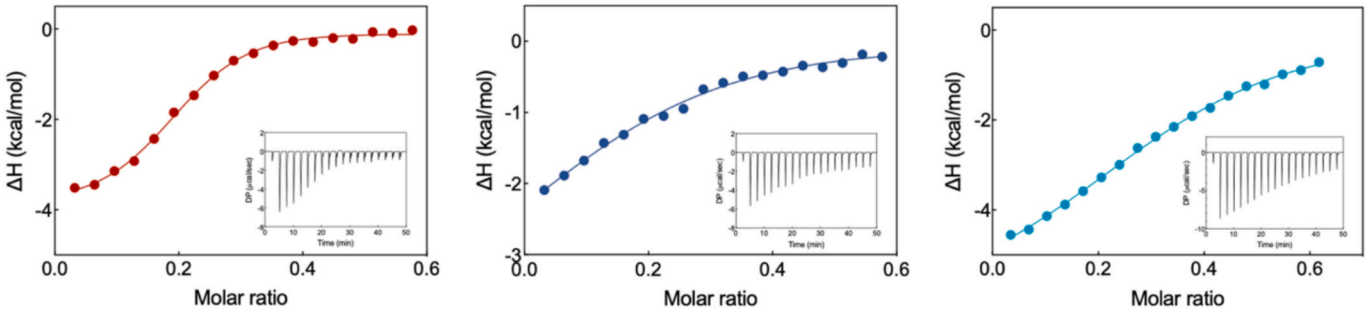

Fig. 3. Integrated heat curves and corresponding raw thermogram (insets) from ITC experiments of HSA titrated with **1@-A**, **1@-TA**, and **1@-COOH**.

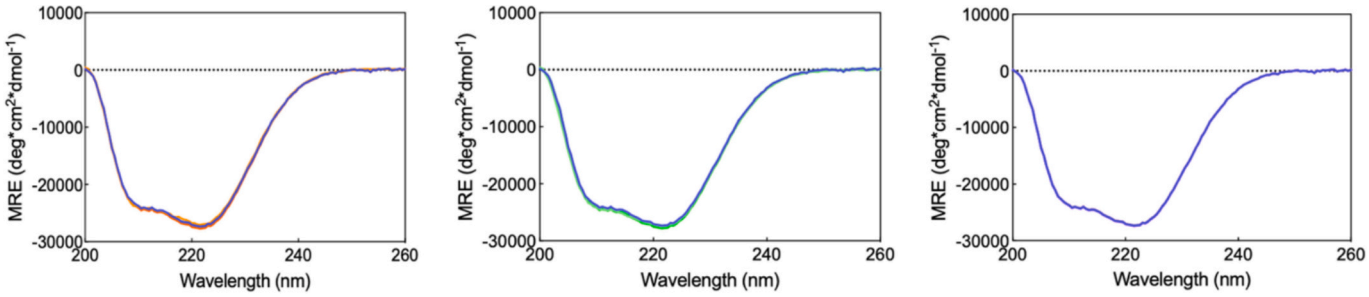

Fig. 4. UV CD spectra of HSA in the absence (blue) and in the presence of: **1-A** (2 μM, orange) and **1@-A** (50 μM, dark orange) (left); **1-TA** (2 μM, light green) and **1@-TA** (50 μM, forest green) (middle); **1-COOH** (2 μM, magenta) and **1@-COOH** (50 μM, purple) (right). Measurements were performed at 298 K in PBS buffer (pH 7.4). (For interpretation of the references to colour in this figure legend, the reader is referred to the web version of this article.)

Table 3
Percentage of α-helical content and melting temperature (T_m) of HSA in the absence and presence of monomeric and nanomicellar AD-PAMAM derivatives, as determined by CD spectroscopy. Data are reported as mean ± SD from 3 independent experiments.

Sample	% α-helix	T_m [K]
HSA	62.6 ± 0.2	338.30 ± 0.49
HSA + 1-A	63.2 ± 0.3	338.87 ± 0.26
HSA + 1@-A	63.6 ± 0.6	337.31 ± 0.32
HSA + 1-TA	63.4 ± 0.3	336.52 ± 0.48
HSA + 1@-TA	63.9 ± 0.4	337.27 ± 0.28
HSA + 1-COOH	62.8 ± 0.7	337.48 ± 0.36
HSA + 1@-COOH	62.5 ± 0.1	338.46 ± 0.31

protein folding, ligand binding, and protein–nanostructure interactions [44,45]. In this study, 3D-FS spectra were recorded for HSA alone and in the presence of all AD-PAMAM derivatives, both in their monomeric and nanomicellar forms. As a representative example, Fig. 5 shows the fluorescence landscapes of HSA in the absence and in the presence of **1-A** (monomeric) and **1@-A** (nanomicellar). The characteristic fluorescence peak ($\lambda_{ex}/\lambda_{em}$ = 280/343 nm), attributed to Trp214 - located in the hydrophobic core of the protein - serves as a sensitive probe for tertiary structure and local polarity [45,46].

As seen in Fig. 5, no substantial shifts in peak position or changes in intensity were observed upon complexation with either **1-A** or **1@-A**. Similar results were obtained for the other ADs (see **Fig. S5**), indicating that none of the derivatives induce significant perturbations in the microenvironment of Trp214. These findings suggest that the interaction with HSA does not result in appreciable conformational rearrangements, in agreement with the CD spectroscopy data discussed above and molecular dynamics analyses, which will be presented in § 3.4.

3.3.3. Size and ζ-potential analysis of HSA–nanomicelle complexes via dynamic light scattering

Dynamic Light Scattering (DLS) is a widely employed technique for characterizing the size and surface charge of nanoscale colloidal systems in solution. It provides key parameters such as hydrodynamic diameter and ζ-potential, offering valuable insights into colloidal stability, surface interactions, and complexation behavior of soft nanomaterials, including protein-nanoparticle assemblies [47]. Here, the hydrodynamic size and surface charge of the HSA/nanomicelle complexes were assessed by DLS under aqueous buffered conditions. The recorded diameters were 15.9 ± 0.3 nm for HSA/**1@-A**, 15.6 ± 0.4 nm for HSA/**1@-TA**, and 14.2 ± 0.6 nm for HSA/**1@-COOH** (Fig. 6), consistent with compact supramolecular architectures. These values closely match the estimated protein-to-nanomicelle stoichiometry derived from thermodynamics and computational analyses (see § 3.4).

ζ-potential measurements revealed distinct electrostatic profiles for the three dendrimer-based/HSA nanoassemblies. Indeed, the complexes formed by HSA with **1@-A** and **1@-TA** exhibited ζ-potential values of **1@-A** and **1@-TA** nanomicelles to +6.1 and + 4.3 mV, respectively, suggesting partial masking of the dendrimeric charge by negatively charged residues HSA surface. In contrast, the complex with **1@-COOH** displayed a ζ-potential of −17.9 mV, consistent with a reversed surface polarity and indicative of strong electrostatic interactions with basic protein domains. Together, these data support a stoichiometry of four HSA molecules per nanomicelle in the **1@-A** and **1@-TA** systems, and three in the case of **1@-COOH**. This composition aligns with previously determined aggregation numbers (N_{agg}) [11], and is further supported by the molar ratio from calorimetric experiment (§ 3.2), molecular dynamics, and comparative experimental data from similar protein–nanoparticle complexes [17,39].

3.4. Computational analysis

3.4.1. Computational characterization of HSA/monomer binding

Molecular dynamics (MD) simulations were firstly employed to investigate the binding interactions between the AD monomers and

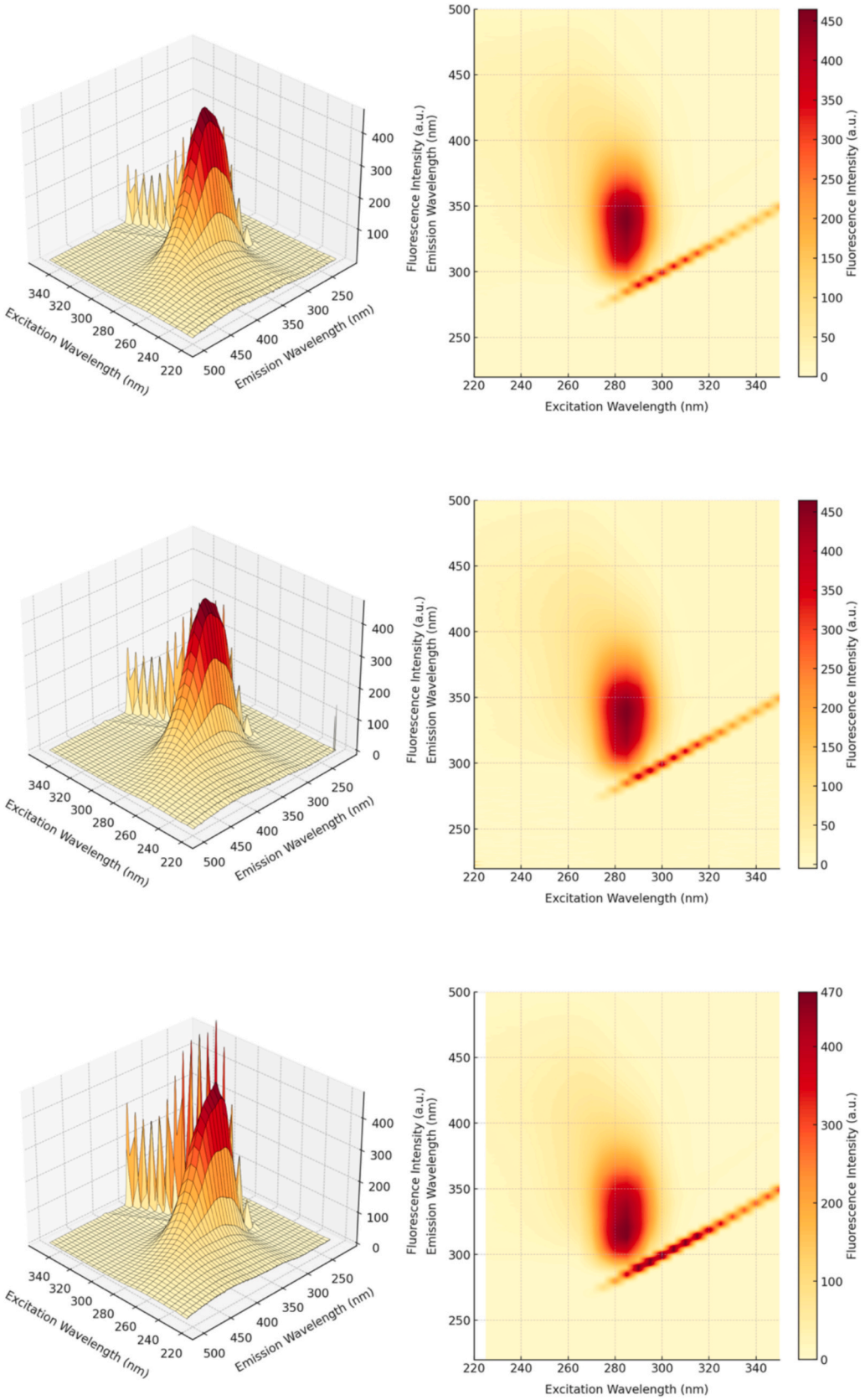

Fig. 5. Three-dimensional fluorescence spectra (left panels) and corresponding two-dimensional contour maps (right panels) of 2 μM HSA in the absence (top row) and presence of the amphiphilic AD-PAMAM derivative, shown in its monomeric (**1-A**, 2 μM, middle row) and nanomicellar (**1@-A**, 50 μM, bottom row) forms.

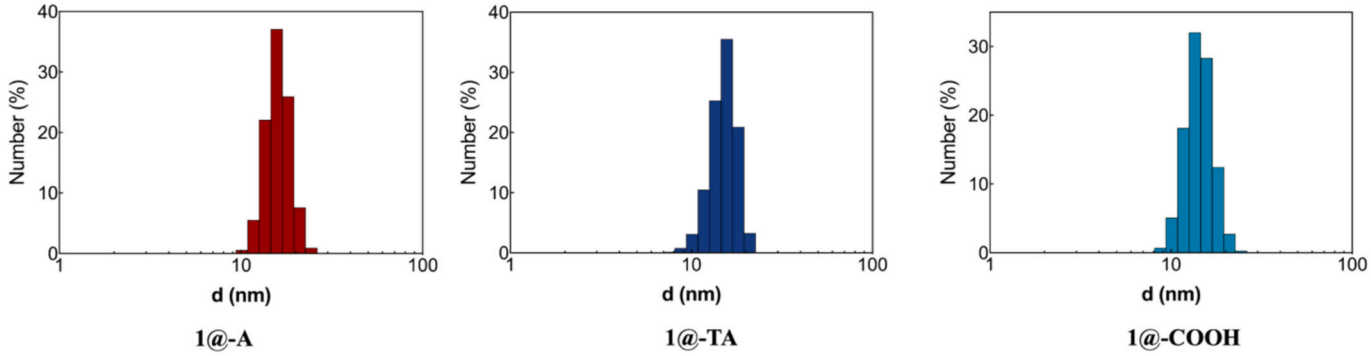

Fig. 6. Hydrodynamic diameter (d) of HSA in complex with **1@-A** (left), **1@-TA** (middle), and **1@-COOH** (right) at 298 K as measured by DLS.

HSA, as well as their potential structural consequences. The results revealed distinct binding features for the AD monomers toward specific fatty acid (FA) pockets in HSA. Specifically, the cationic derivatives **1-A** and **1-TA** preferentially occupied the FA7 pocket, which overlaps structurally with Sudlow's site I [21], while the anionic monomer **1-COOH** engaged the FA5 site, located in a basic residue-rich region [21]. Competitive fluorescence assays were carried out to validate the docking/MD-predicted binding sites. HSA quenching was monitored in the presence of canonical site markers. Warfarin (FA7) reduced the apparent K_{SV} for **1-A** and **1-TA**, whereas stearic acid (FA5) reduced K_{SV} for **1-COOH** and produced no appreciable effect on **1-A**/**1-TA**. This reciprocal pattern supports the site-selective engagement inferred from docking/MD (**1-A**/**1-TA** at FA7/ and **1-COOH** at FA5). Detailed values of K_{SV} are provided in **Table S2**. All three binding modes were stable over 200 ns of MD simulation, as evidenced by backbone RMSD plateaus and the plot of the radius of gyration (R_g) over the production window (**Fig. S6** and Fig. 7). As shown in Fig. 7 (upper panels), the ligands remained consistently anchored within the selected pockets throughout the trajectory. In each case, the hydrophobic C_{18} tail was deeply embedded in the protein cleft, minimizing solvent exposure and contributing significantly to complex stabilization through persistent hydrophobic interactions. The polar head groups of **1-A** and **1-TA** remained exposed to the solvent and formed only transient contacts with the protein surface (Fig. 7, upper left and center). In contrast, the negatively charged head group of **1-COOH** penetrated deeper into the binding cleft, in line with the distribution of internal basic residues (Fig. 7, upper right). Despite these localized interactions, none of the trajectories showed persistent hydrogen bonds or stable salt bridges, indicating that hydrophobic burial of the alkyl chain constitutes the primary stabilizing force. Critically, the binding modes observed in silico align with the thermodynamic signatures obtained by ITC (§3.2), corroborating both the identity of the binding pockets and the relative

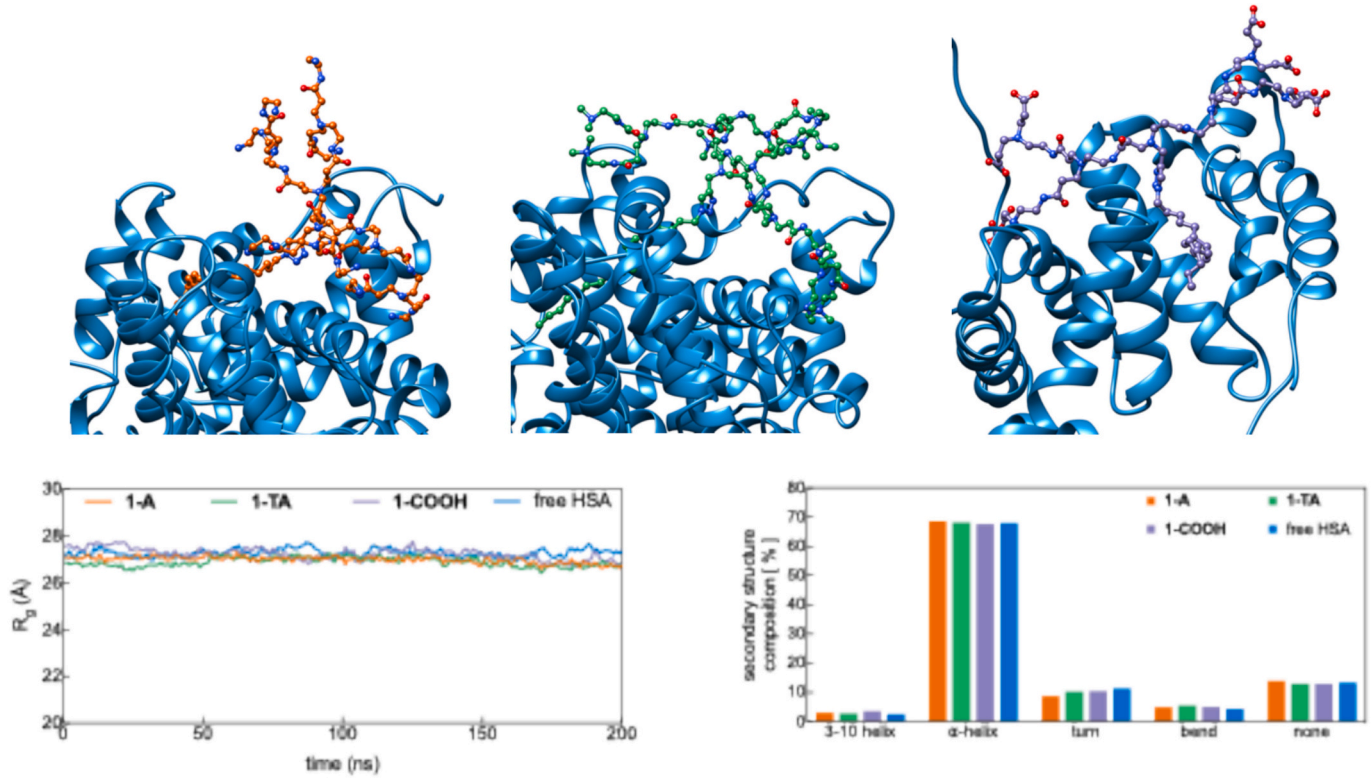

Fig. 7. (Upper panels) Final MD snapshots of **1-A** (left), **1-TA** (center), and **1-COOH** (right) bound to HSA within the fatty acid binding region. The AD monomers are shown in ball-and-stick representation (O: red; N: blue; C: orange, green and purple, respectively). The HSA is rendered in blue. Hydrogen atoms, water molecules, and ions are omitted for clarity. (Lower left panel) Radius of gyration of HSA over time during the MD simulations in complex with each dendrimer monomer. (Lower right panel) Secondary structure content of HSA, averaged over the last 100 ns of simulation, for both free and bound protein systems.

affinities of the three monomers.

To evaluate potential structural effects of monomer binding, global metrics such as R_g and secondary structure content were monitored throughout the simulations (Fig. 7, lower panels). The R_g of unbound HSA remained stable at 27.27 ± 0.18 Å, consistent with reported values [48,49]. Complexation with **1-A**, **1-TA**, and **1-COOH** resulted in comparable R_g values (26.99 ± 0.14, 26.89 ± 0.19, and 27.24 ± 0.24 Å, respectively), indicating no loss of compactness (Fig. 7, lower left panel). Secondary structure profiles were likewise preserved across all systems (Fig. 7, lower right panel), confirming that the overall protein fold remains unaffected. These observations align closely with the CD spectroscopy data (§3.3.1), reinforcing the conclusion that AD-PAMAM monomer binding does not compromise the structural integrity of HSA.

3.4.2. Computational analysis of structural properties of HSA/AD-PAMAM nanomicelle complexes

The structural integrity of the nanomicelles in complex with HSA was also assessed through all-atom MD simulations. R_g and asphericity analyses indicated that both size and overall shape were largely preserved upon protein binding. As shown in Fig. 8 (upper panel), R_g values increased modestly – by approximately 1 Å - following complexation, consistent across all three systems. In detail, for the free nanomicelles average R_g values were 22.56 ± 0.40 Å (**1@-A**), 24.06 ± 0.55 Å (**1@-TA**), and 15.43 ± 0.19 Å (**1@-COOH**). Upon binding to HSA, the values shifted to 23.47 ± 0.33 Å, 24.63 ± 0.21 Å, and 16.51 ± 0.15 Å, respectively. These minimal variations support the retention of nanomicelle compactness in the presence of the protein.

Asphericity values, calculated from the principal moments of the gyration tensor, remained low and comparable between free and HSA-bound nanomicelles, confirming that the overall spherical morphology is retained upon complexation. Average values of 0.11 ± 0.04, 0.07 ± 0.04, and 0.06 ± 0.03 for the free **1@-A**, **1@-TA**, and **1@-COOH** nanomicelles increased only slightly in the corresponding complexes (0.14 ± 0.03, 0.09 ± 0.02, and 0.06 ± 0.02, respectively). These results indicate that nanomicelle architecture remains robust in the presence of a protein corona, likely due to uniform surface coverage and isotropic interactions involving the dendrimer termini, which prevent the asymmetric deformations often observed in protein–nanoparticle systems. From the protein's perspective, nanomicelle binding has no discernible impact on overall size or compactness, as evidenced by stable backbone RMSD plateaus and an essentially invariant R_g over the equilibrated window (**Fig. S7** and Fig. 8). Indeed, the R_g of HSA in the complexes ranged from 26.53 to 27.20 Å (with standard deviation ≤0.16 Å), closely matching that of the unbound protein (27.01 ± 0.18 Å) and previously reported values under comparable conditions [48,49]. To assess possible conformational changes, secondary structure profiles of HSA were analyzed using the DSSP algorithm [50]. In the unbound state, the protein exhibited 68.0 % α-helix and 11.5 % turns, with no detectable β-sheet content, consistent with established structural data [51]. Upon nanomicelle binding, the α-helical content remained within 65.5–69.4 %, and turn content varied between 8.8 % and 10.6 %, again without β-sheet formation. These results (Fig. 8, lower panel) confirm that the native fold of HSA is preserved in all complexes, with no evidence of structural destabilization.

To characterize the structural and electrostatic properties of the HSA-nanomicelle complexes at atomistic resolution, their size, surface potential, and internal organization were systematically analyzed. The R_g of the complexes revealed similar values for the positively charged nanomicelles: 50.64 ± 0.62 Å for HSA/**1@-A** and 48.97 ± 0.70 Å for HSA/**1@-TA**, indicating comparable degrees of compaction. In contrast, the HSA/**1@-COOH** complex exhibited a smaller R_g (42.64 ± 0.56 Å), consistent with the reduced number of HSA molecules forming its corona. To further assess electrostatic behavior, surface-averaged electrostatic potentials (SAEP) were computed and used to estimate effective zeta potentials. HSA alone was predicted to carry a ζ-potential of approximately −11.5 mV, in line with experimental reports [17,52]. Upon HSA complexation, **1@-A** and **1@-TA** retained net positive potentials (+5.94 mV and + 6.00 mV, respectively), reflecting partial charge neutralization by HSA while preserving a cationic surface. This behavior is consistent with a binding mode in which negatively charged HSA regions face the dendrimer core, leaving cationic domains exposed to the solvent. In contrast, the **1@-COOH** complex displayed a ζ-potential of −14.4 mV, suggesting preferential interaction of the dendrimer's terminal carboxylates with localized basic patches on HSA, while exposing anionic protein surfaces. The internal structure of the nanomicelles and their interfacial organization were also examined by radial distribution function (RDF) analysis, calculated relative to both the nanomicelle center of mass. As shown in **Fig. S8** the micellar core remained stable in all systems, particularly for the cationic dendrimers. In the HSA/**1@-COOH** complex, a slight expansion of the nanomicelle surface was observed, attributed to outward extension of the flexible anionic branches toward nearby cationic domains on the protein.

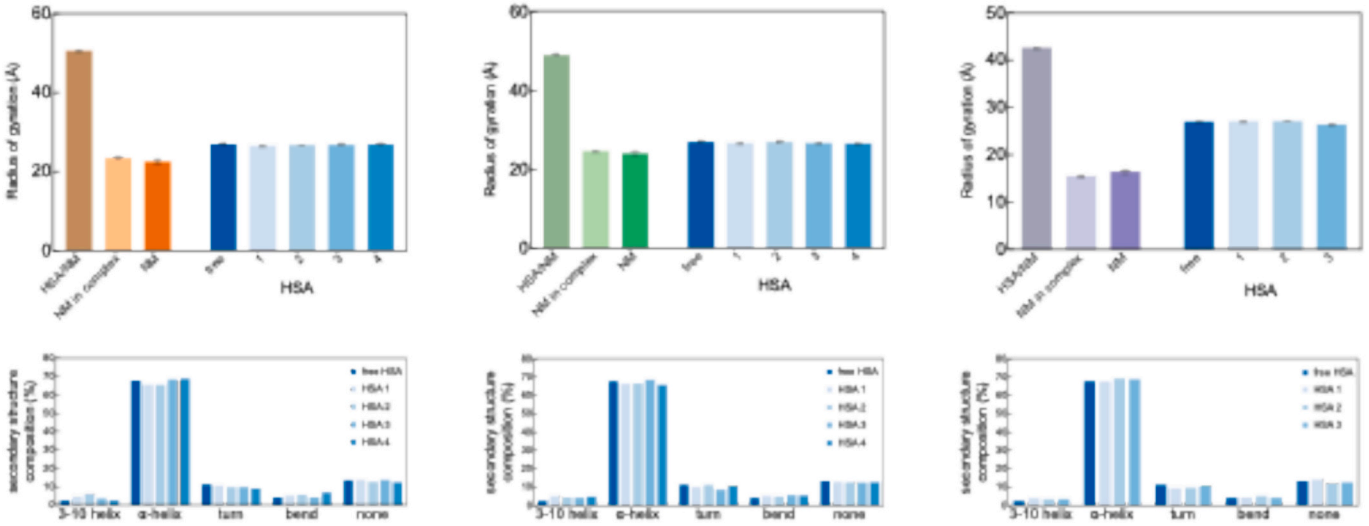

Fig. 8. (Upper panels) Radius of gyration (R_g) for each system: free HSA, free nanomicelle, full complex, and individual HSA chains within the complex. Left to right: **1@-A** (four HSA chains), **1@-TA** (four HSA chains), and **1@-COOH** (three HSA chains). (Lower panels) Secondary structure content of free HSA and of the individual HSA chains in the corresponding nanomicellar complexes.

3.4.3. Computational characterization of HSA/nanomicelles binding

Protein–nanomicelle interfaces were analyzed by quantifying atomic contacts between individual HSA residues and nanomicelle atoms along the MD trajectories. For each frame, the minimum distance between every residue and any nanomicelle atom was calculated (**Fig. S9**). Contact analysis revealed consistent interaction profiles among the HSA molecules within a given corona, and across complexes formed with nanomicelles of similar charge. Contact frequency maps were generated by defining a contact as any interatomic distance $\leq$ 6.5 Å (Fig. 9). These maps provided residue-level interaction fingerprints, which, while generally non-specific, exhibited clear differences depending on nanomicelle charge. Binding free energy decompositions using MM-GBSA were performed to evaluate the energetic contributions of individual HSA residues (**Fig. S10**). A strong correlation was observed between contact frequency and binding energy profiles across all systems, reinforcing the reliability of the interaction maps. Electrostatic interactions were identified as the dominant driving force in all complexes.

Stable salt bridges and polar contacts between nanomicelle branches and HSA residues were analyzed to further characterize the nature of the interaction. Approximately 80 % of the charged dendrimer terminals in **1@-A** and **1@-TA** formed salt bridges persisting for more than 50 % of the trajectory, whereas only 40 % of branches in **1@-COOH** engaged in such interactions. This lower frequency reflects the limited availability of basic residues on the HSA surface. In contrast, polar contacts involving oxygen and nitrogen atoms were more common in **1@-COOH** (25 %) than in **1@-TA** (10 %) and **1@-A** (6 %). The broader charge distribution of **1@-TA** likely reduces salt bridge persistence, favoring alternative polar interactions. Notably, **1@-A** exhibited the most stable salt bridges, with ~50 % persisting for over 95 % of the simulation, compared to ~33 % in **1@-TA**. These results indicate that both charge localization and dendrimer flexibility modulate the dynamic nature of AD nanomicelle–protein binding. In addition to electrostatic and polar interactions, extensive van der Waals contacts contributed to complex stabilization. Overall, binding appears to occur through a flexible, non-specific interface driven by a combination of electrostatic, polar, and hydrophobic forces, rather than by defined docking sites. At the residue level, interaction profiles of the cationic nanomicelles showed a preference for surface-exposed, negatively charged helices on HSA, particularly those spanning residues E252–D259 and E266–D269 (Fig. 10).

In contrast, the negatively charged **1@-COOH** nanomicelle penetrated more deeply into the protein, establishing stable contacts with internal residues such as K195. Radial distribution analyses (**Fig. S11**) supported this observation, showing that charged atoms of **1@-COOH** approached the HSA center of mass to within ~11 Å, whereas those of **1@-A** and **1@-TA** remained beyond 20 Å. Visualization of contact frequencies (Fig. 9, left panels) confirmed this trend: while positively charged nanomicelles primarily engaged surface residues, **1@-COOH** accessed more buried regions of the protein. This deeper insertion likely accounts for the reduced number of HSA molecules in the **1@-COOH** corona. Internal binding limits the availability of dendrimer branches for additional interactions, favoring the formation of compact, three-protein complexes despite a comparable nanomicelle surface area.

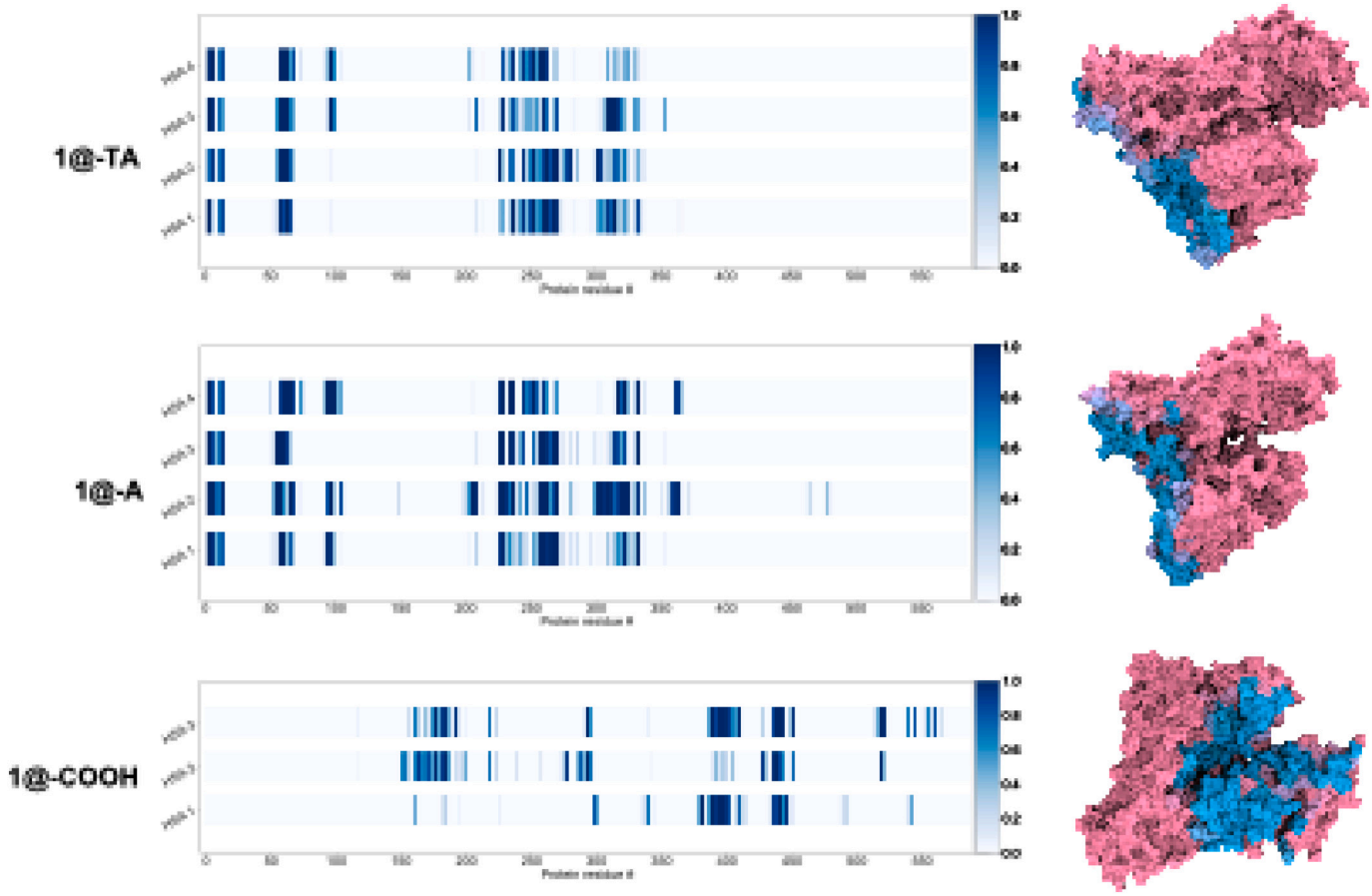

Fig. 9. (Left panel) Residue-level contact frequency maps for the HSA–nanomicelle complexes, computed along the MD trajectories. Darker bars indicate higher contact persistence (defined as interatomic distance $\leq$ 6.5 Å). Rows correspond to individual HSA chains within each complex. (Right panel) Solvent-accessible surface representations of one representative HSA molecule per complex, colored by residue contact frequency with the nanomicelle. Residues not involved in interactions are shown in pink; residues with persistent contacts are highlighted in cyan. (For interpretation of the references to colour in this figure legend, the reader is referred to the web version of this article.)

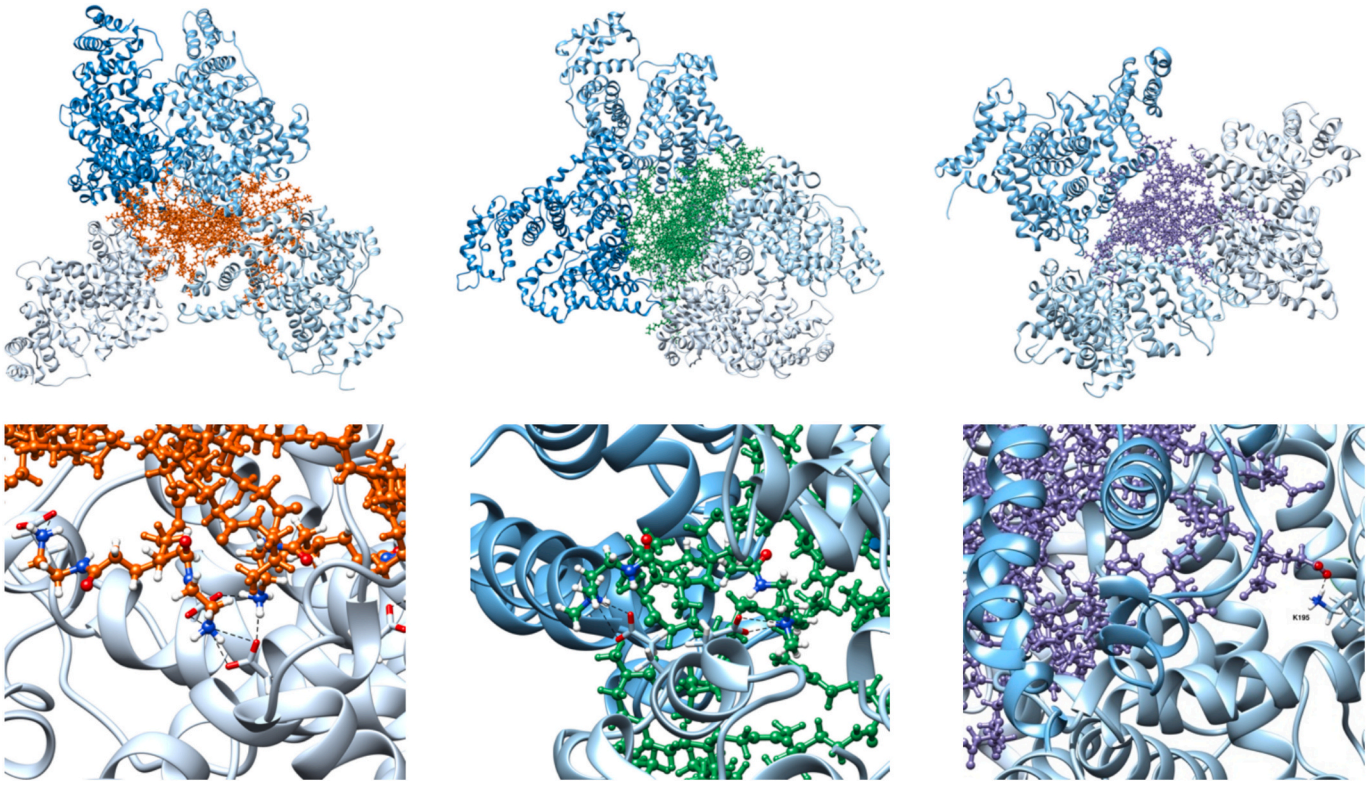

Fig. 10. (Top panel) Representative MD snapshots of the HSA–nanomicelle complexes. HSA is shown in cartoon representation, with individual chains colored in in different shades of blue. Nanomicelles are depicted as sticks and balls, with dendrimer branches colored in orange (**1@-A**, left), green (**1@-TA**, center), and purple (**1@-COOH**, right). (Bottom panel) Zoomed-in views highlighting representative polar and electrostatic interactions between nanomicelle branches and selected HSA residues. Key residues involved in persistent salt bridges or hydrogen bonding are shown as dotted lines. All images omit water molecules, ions and counterions for clarity.

4. Conclusion

This study provides a comprehensive molecular-level characterization of the interaction between human serum albumin and PAMAM-based amphiphilic dendrimers, examined in both monomeric and self-assembled nanomicellar forms. Through an integrated experimental and computational approach, binding affinity, thermodynamic signatures, structural effects, and interfacial organization were systematically evaluated. Micellization was found to markedly enhance HSA binding affinity, primarily via multivalent electrostatic interactions. Isothermal titration calorimetry revealed dissociation constants in the low micromolar range for nanomicelle–HSA complexes, in contrast to the significantly weaker interactions observed for monomeric dendrons. Thermodynamic profiling indicated distinct binding modes: entropy-driven in monomers, and enthalpically stabilized in nanomicelles, consistent with the formation of extended interfacial contacts. Spectroscopic data, including fluorescence quenching, circular dichroism, and 3D fluorescence spectroscopy, confirmed that binding occurs without significant perturbation of the secondary or tertiary structure of the serum protein, supporting a non-disruptive, surface-localized interaction. Atomistic molecular dynamics simulations further reinforced these observations, detailing the organization of protein coronas and identifying the residues most involved in complex stabilization. More specifically, converging evidence from spectroscopy, calorimetry, and MD indicates weak association for monomers and modest–moderate association for nanomicelles, consistent with a soft, reversible corona and limited structural perturbation of HSA. Under the conditions tested, no major impact on HSA functional competence is anticipated. Future studies will implement dedicated functional assays (e.g., ligand-transport/displacement and esterase-like readouts) to quantify any subtle effects.

Speaking about the plausible formation of the protein corona in this system, the protein–nanoparticle interface is best described as a soft rather than hard corona. The measured dissociation constants indicate moderate and reversible association, which is not compatible with the strong, quasi-irreversible adsorption typical of hard coronas but is consistent with transient, dynamic contacts [53]. In addition, the nanoparticles display a small hydrodynamic diameter (~15 nm), comparable to that of many serum proteins; as reported in the literature, when nanoparticle size approaches that of the protein, the resulting high surface curvature limits the number of simultaneous contact points and reduces adsorption energy, favoring weak, reversible interactions and heteroaggregation-like behavior rather than the formation of a stable, hard corona [54]. Taken together, these elements support a soft, dynamic corona, with proteins exchanging rapidly with those in the surrounding medium.

Collectively, the results highlight the key role of supramolecular architecture and surface charge distribution in modulating protein recognition. Positively charged nanomicelles engaged up to four HSA molecules, while negatively charged systems favored three-HSA coronas, underscoring the impact of nanoscale presentation on binding stoichiometry and dynamics.

These insights provide a robust foundation for the rational design of dendritic nanocarriers with tunable interfacial properties. Future investigations should explore the behavior of such systems under biologically relevant conditions, including competitive protein adsorption and complex media. Extending this framework to in vivo studies may clarify how protein corona formation influences circulation, immune recognition, and the overall therapeutic profile of dendritic nanostructures.

CRediT authorship contribution statement

Gabriele Cavalieri: Writing – review & editing, Writing – original draft, Visualization, Validation, Investigation, Data curation. **Domenico Marson:** Writing – review & editing, Writing – original draft, Software, Investigation, Data curation. **Dinesh Dhumal:** Writing – review & editing, Validation, Investigation. **Ling Peng:** Writing – review & editing, Visualization, Supervision, Investigation. **Erik Laurini:** Writing – review & editing, Writing – original draft, Supervision, Project administration, Funding acquisition, Data curation, Conceptualization. **Sabrina Pricl:** Writing – review & editing, Writing – original draft, Supervision, Funding acquisition, Conceptualization.

Declaration of competing interest

The authors declare that they have no known competing financial interests or personal relationships that could have appeared to influence the work reported in this paper.

Acknowledgments

This work was supported by ICSC – Centro Nazionale di Ricerca in High-Performance Computing, Big Data, and Quantum Computing (Spoke 7, WP4 Pilot Applications, and T.2.8 Development and optimization of HPC-based integrated workflows based on flagship codes for personalized (nano)medicine). S.P. also acknowledges financial support from the Italian Association for Cancer Research (AIRC, grant IG17413 Novel hot-spot mutations in BCR-ABL1: role in resistance to CML target therapy), the Friuli Venezia Giulia Region (REFVG, grant Study of the oncogene B-Raf and its mutation for the selection of melanoma patients eligible for targeted therapies with specific inhibitors – No-Mel), and Fondazione Cassa di Risparmio di Trieste (Fondazione CRTrieste, grant Far-UV CD spectroscopy in translational medicine).

The authors gratefully acknowledge the CINECA award under the ISCRA initiative (proposal NoOneOut, HP10BPK7ZX) for the availability of high-performance computing resources and technical support.

Appendix A. Supplementary data

Supplementary data to this article can be found online at https://doi.org/10.1016/j.molliq.2025.128770.

Data availability

Data will be made available on request.

References

[1] C.S. Ho, C.T.H. Wong, T.T. Aung, R. Lakshminarayanan, J.S. Mehta, S. Rauz, A. McNally, B. Kintses, S.J. Peacock, C. De La Fuente-Nunez, R.E.W. Hancock, D.S. J. Ting, Antimicrobial resistance: a concise update, The Lancet Microbe 6 (2025) 100947, https://doi.org/10.1016/j.lanmic.2024.07.010.

[2] D. Dhumal, B. Maron, E. Malach, Z. Lyu, L. Ding, D. Marson, E. Laurini, A. Tintaru, B. Ralahy, S. Giorgio, S. Pricl, Z. Hayouka, L. Peng, Dynamic self-assembling supramolecular dendrimer nanosystems as potent antibacterial candidates against drug-resistant bacteria and biofilms, Nanoscale 14 (2022) 9286–9296, https://doi.org/10.1039/D2NR02305A.

[3] N. Zhang, D. Dhumal, S.H. Kuo, S.Q. Lew, P.D. Patil, R. Taher, S. Vaidya, C. Galanakou, A. Elkihel, M.W. Oh, S.Y. Chong, D. Marson, J. Zheng, O. Rouvinski, W.O. Abolarin, S. Pricl, G.W. Lau, L.T.O. Lee, L. Peng, Targeting the phosphatidylglycerol lipid: an amphiphilic dendrimer as a promising antibacterial candidate, Sci. Adv. 10 (2024) eadn8117, https://doi.org/10.1126/sciadv.adn8117.

[4] N. King, D. Dhumal, S.Q. Lew, S.H. Kuo, C. Galanakou, M.W. Oh, S.Y. Chong, N. Zhang, L.T.O. Lee, Z. Hayouka, L. Peng, G.W. Lau, Amphiphilic dendrimer as potent antibacterial against drug-resistant bacteria in mouse models of human infectious diseases, ACS Infect. Dis. 10 (2024) 453–466, https://doi.org/10.1021/acsinfecdis.3c00425.

[5] M. Mahmoudi, M.P. Landry, A. Moore, R. Coreas, The protein corona from nanomedicine to environmental science, Nat. Rev. Mater. 8 (2023) 422–438, https://doi.org/10.1038/s41578-023-00552-2.

[6] A. Guglielmelli, P. D'Aquila, G. Palermo, M. Dell'Aglio, G. Passarino, G. Strangi, D. Bellizzi, Role of the human serum albumin protein Corona in the antimicrobial and Photothermal activity of metallic nanoparticles against *Escherichia coli* Bacteria, ACS Omega 8 (2023) 31333–31343, https://doi.org/10.1021/acsomega.3c03774.

[7] A.O. Elzoghby, W.M. Samy, N.A. Elgindy, Albumin-based nanoparticles as potential controlled release drug delivery systems, J. Control. Release 157 (2012) 168–182, https://doi.org/10.1016/j.jconrel.2011.07.031.

[8] X. Liu, D. Dhumal, P. Santofimia-Castaño, J. Liu, M. Casanova, A.C. Garcia-Muñoz, T.-A. Perles-Barbacaru, A. Elkihel, W. Zhang, T. Roussel, C. Galanakou, J. Wu, E. Zerva, N. Dusetti, Y. Xia, X.-J. Liang, A. Viola, J.L. Iovanna, L. Peng, Self-assembling dendrimer nanodrug formulations for decreased hERG-related toxicity and enhanced therapeutic efficacy, Sci. Adv. 11 (2025), https://doi.org/10.1126/sciadv.adu9948.

[9] Y. Jiang, Z. Lyu, B. Ralahy, J. Liu, T. Roussel, L. Ding, J. Tang, A. Kosta, S. Giorgio, R. Tomasini, X.-J. Liang, N. Dusetti, J. Iovanna, L. Peng, Dendrimer nanosystems for adaptive tumor-assisted drug delivery via extracellular vesicle hijacking, Proc. Natl. Acad. Sci. USA 120 (2023), https://doi.org/10.1073/pnas.2215308120.

[10] C. Chen, P. Posocco, X. Liu, Q. Cheng, E. Laurini, J. Zhou, C. Liu, Y. Wang, J. Tang, V.D. Col, T. Yu, S. Giorgio, M. Fermeglia, F. Qu, Z. Liang, J.J. Rossi, M. Liu, P. Rocchi, S. Pricl, L. Peng, Mastering dendrimer self-assembly for efficient siRNA delivery: from conceptual design to in vivo efficient gene silencing, Small 12 (2016) 3667–3676, https://doi.org/10.1002/smll.201503866.

[11] D. Dhumal, W. Lan, L. Ding, Y. Jiang, Z. Lyu, E. Laurini, D. Marson, A. Tintaru, N. Dusetti, S. Giorgio, J.L. Iovanna, S. Pricl, L. Peng, An ionizable supramolecular dendrimer nanosystem for effective siRNA delivery with a favorable safety profile, Nano Res 14 (2021) 2247–2254, https://doi.org/10.1007/s12274-020-3216-8.

[12] T. Yu, X. Liu, A. Bolcato-Bellemin, Y. Wang, C. Liu, P. Erbacher, F. Qu, P. Rocchi, J. Behr, L. Peng, An amphiphilic dendrimer for effective delivery of small interfering RNA and gene silencing in vitro and in vivo, Angew. Chem. Int. Ed. 51 (2012) 8478–8484, https://doi.org/10.1002/anie.201203920.

[13] C. Leggio, L. Galantini, N.V. Pavel, About the albumin structure in solution: cigar expanded form versus heart Normal shape, Phys. Chem. Chem. Phys. 10 (2008) 6741, https://doi.org/10.1039/b808938h.

[14] C.N. Pace, F. Vajdos, L. Fee, G. Grimsley, T. Gray, How to measure and predict the molar absorption coefficient of a protein, Protein Sci. 4 (1995) 2411–2423, https://doi.org/10.1002/pro.5560041120.

[15] J.R. Lakowicz, Principles of Fluorescence Spectroscopy, 3rd ed, Springer, New York, 2006.

[16] K.A. Thornalley, E. Laurini, S. Pricl, D.K. Smith, Enantiomeric and Diastereomeric self-assembled multivalent nanostructures: understanding the effects of chirality on binding to Polyanionic heparin and DNA, Angew. Chem. Int. Ed. 57 (2018) 8530–8534, https://doi.org/10.1002/anie.201803298.

[17] G. Cavalieri, D. Marson, N. Giurgevich, R. Valeri, F. Felluga, E. Laurini, S. Pricl, Molecular ballet: investigating the complex interaction between self-assembling dendrimers and human serum albumin via computational and experimental methods, Pharmaceutics 16 (2024) 533, https://doi.org/10.3390/pharmaceutics16040533.

[18] N.E. Olesen, R. Holm, P. Westh, Determination of the aggregation number for micelles by isothermal titration calorimetry, Thermochim. Acta 588 (2014) 28–37, https://doi.org/10.1016/j.tca.2014.04.028.

[19] ITC for characterization of self-assembly process of cationic Dendrons for siRNA delivery, in: Methods in Molecular Biology, Springer US, New York, NY, 2021, pp. 245–266, https://doi.org/10.1007/978-1-0716-1298-9_15.

[20] M. Russi, R. Valeri, D. Marson, C. Danielli, F. Felluga, A. Tintaru, N. Skoko, S. Aulic, E. Laurini, S. Pricl, Some things old, new and borrowed: delivery of dabrafenib and vemurafenib to melanoma cells via self-assembled nanomicelles based on an amphiphilic dendrimer, Eur. J. Pharm. Sci. 180 (2023) 106311, https://doi.org/10.1016/j.ejps.2022.106311.

[21] E. Johansson, A.D. Nielsen, H. Demuth, C. Wiberg, C.B. Schjødt, T. Huang, J. Chen, S. Jensen, J. Petersen, P. Thygesen, Identification of binding sites on human serum albumin for Somapacitan, a long-acting growth hormone derivative, Biochemistry 59 (2020) 1410–1419, https://doi.org/10.1021/acs.biochem.0c00019.

[22] W. Rocchia, E. Alexov, B. Honig, Extending the applicability of the nonlinear Poisson−Boltzmann equation: multiple dielectric constants and multivalent ions, J. Phys. Chem. B 105 (2001) 6507–6514, https://doi.org/10.1021/jp010454y.

[23] O. Trott, A.J. Olson, AutoDock Vina: improving the speed and accuracy of docking with a new scoring function, efficient optimization, and multithreading, J. Comput. Chem. 31 (2010) 455–461, https://doi.org/10.1002/jcc.21334.

[24] J. Wang, R.M. Wolf, J.W. Caldwell, P.A. Kollman, D.A. Case, Development and testing of a general amber force field, J. Comput. Chem. 25 (2004) 1157–1174, https://doi.org/10.1002/jcc.20035.

[25] E. Vanquelef, S. Simon, G. Marquant, E. Garcia, G. Klimerak, J.C. Delepine, P. Cieplak, F.-Y. Dupradeau, R.E.D. Server, a web service for deriving RESP and ESP charges and building force field libraries for new molecules and molecular fragments, Nucleic Acids Res. 39 (2011) W511–W517, https://doi.org/10.1093/nar/gkr288.

[26] Y. Wang, H. Yu, X. Shi, Z. Luo, D. Lin, M. Huang, Structural mechanism of ring-opening reaction of glucose by human serum albumin, J. Biol. Chem. 288 (2013) 15980–15987, https://doi.org/10.1074/jbc.M113.467027.

[27] J.A. Maier, C. Martinez, K. Kasavajhala, L. Wickstrom, K.E. Hauser, C. Simmerling, ff14SB: improving the accuracy of protein side chain and backbone parameters from ff99SB, J. Chem. Theory Comput. 11 (2015) 3696–3713, https://doi.org/10.1021/acs.jctc.5b00255.

[28] A. Chakravorty, Z. Jia, L. Li, E. Alexov, A new DelPhi feature for modeling electrostatic potential around proteins: role of bound ions and implications for

zeta-potential, Langmuir 33 (2017) 2283–2295, https://doi.org/10.1021/acs.langmuir.6b04430.
[29] W.L. Jorgensen, J. Chandrasekhar, J.D. Madura, R.W. Impey, M.L. Klein, Comparison of simple potential functions for simulating liquid water, J. Chem. Phys. 79 (1983) 926–935, https://doi.org/10.1063/1.445869.
[30] E. Wang, H. Sun, J. Wang, Z. Wang, H. Liu, J.Z.H. Zhang, T. Hou, End-point binding free energy calculation with MM/PBSA and MM/GBSA: strategies and applications in drug design, Chem. Rev. 119 (2019) 9478–9508, https://doi.org/10.1021/acs.chemrev.9b00055.
[31] B.R. Miller, T.D. McGee, J.M. Swails, N. Homeyer, H. Gohlke, A.E. Roitberg, *MMPBSA.py* : an efficient program for end-state free energy calculations, J. Chem. Theory Comput. 8 (2012) 3314–3321, https://doi.org/10.1021/ct300418h.
[32] D.R. Roe, T.E. Cheatham, PTRAJ and CPPTRAJ: software for processing and analysis of molecular dynamics trajectory data, J. Chem. Theory Comput. 9 (2013) 3084–3095, https://doi.org/10.1021/ct400341p.
[33] D.A. Case, H.M. Aktulga, K. Belfon, I.Y. Ben-Shalom, J.T. Berryman, S.R. Brozell, D. S. Cerutti, T.E. Cheatham III, G.A. Cisneros, V.W.D. Cruzeiro, T.A. Darden, N. Forouzesh, G. Giambaşu, T. Giese, M.K. Gilson, H. Gohlke, A.W. Goetz, J. Harris, S. Izadi, S.A. Izmailov, K. Kasavajhala, M.C. Kaymak, E. King, A. Kovalenko, T. Kurtzman, T.S. Lee, P. Li, C. Lin, J. Liu, T. Luchko, R. Luo, M. Machado, V. Man, M. Manathunga, K.M. Merz, Y. Miao, O. Mikhailovskii, G. Monard, H. Nguyen, K. A. O'Hearn, A. Onufriev, F. Pan, S. Pantano, R. Qi, A. Rahnamoun, D.R. Roe, A. Roitberg, C. Sagui, S. Schott-Verdugo, A. Shajan, J. Shen, C.L. Simmerling, N. R. Skrynnikov, J. Smith, J. Swails, R.C. Walker, J. Wang, J. Wang, H. Wei, X. Wu, Y. Wu, Y. Xiong, Y. Xue, D.M. York, S. Zhao, Q. Zhu, P.A. Kollman, Amber 2023, University of California, San Francisco, 2023.
[34] A. Sułkowska, Interaction of drugs with bovine and human serum albumin, J. Mol. Struct. 614 (2002) 227–232, https://doi.org/10.1016/S0022-2860(02)00256-9.
[35] M. Van De Weert, C. Schönbeck, Ligand binding to proteins – when flawed fluorescence quenching methodology and interpretation become the new norm, Eur. J. Pharm. Sci. 203 (2024) 106930, https://doi.org/10.1016/j.ejps.2024.106930.
[36] B. Valeur, Molecular Fluorescence: principles and Applications, Wiley-VCH, Weinheim, 2002.
[37] P.R. Callis, Binding phenomena and fluorescence quenching. I: descriptive quantum principles of fluorescence quenching using a supermolecule approach, J. Mol. Struct. 1077 (2014) 14–21, https://doi.org/10.1016/j.molstruc.2014.04.050.
[38] G. Cavalieri, D. Marson, A. Starz, E. Laurini, S. Pricl, Molecular interactions of Cobimetinib and Vemurafenib with human serum albumin: a comparative biophysical and computational analysis, Mol. Pharm. 22 (2025) 4969–4982, https://doi.org/10.1021/acs.molpharmaceut.5c00625.
[39] T. Cedervall, I. Lynch, S. Lindman, T. Berggård, E. Thulin, H. Nilsson, K.A. Dawson, S. Linse, Understanding the nanoparticle–protein corona using methods to quantify exchange rates and affinities of proteins for nanoparticles, Proc. Natl. Acad. Sci. USA 104 (2007) 2050–2055, https://doi.org/10.1073/pnas.0608582104.
[40] M. Mahmoudi, I. Lynch, M.R. Ejtehadi, M.P. Monopoli, F.B. Bombelli, S. Laurent, Protein−nanoparticle interactions: opportunities and challenges, Chem. Rev. 111 (2011) 5610–5637, https://doi.org/10.1021/cr100440g.
[41] H. Su, Y. Xu, Application of ITC-based characterization of thermodynamic and kinetic Association of Ligands with Proteins in drug design, Front. Pharmacol. 9 (2018) 1133, https://doi.org/10.3389/fphar.2018.01133.
[42] S.M. Kelly, T.J. Jess, N.C. Price, How to study proteins by circular dichroism, Biochimica et Biophysica Acta (BBA) - Proteins and Proteomics 1751 (2005) 119–139, https://doi.org/10.1016/j.bbapap.2005.06.005.
[43] J. Juárez, P. Taboada, V. Mosquera, Existence of different structural intermediates on the fibrillation pathway of human serum albumin, Biophys. J. 96 (2009) 2353–2370, https://doi.org/10.1016/j.bpj.2008.12.3901.
[44] N. Zelenović, P. Ristić, N. Polović, T. Todorović, M. Kojadinović, M. Popović, A multi-spectroscopic and molecular docking analysis of the biophysical interaction between food polyphenols, Urolithins, and Human Serum Albumin, Molecules 29 (2024) 4474, https://doi.org/10.3390/molecules29184474.
[45] F.H. Dos Santos Rodrigues, G.G. Delgado, T. Santana Da Costa, L. Tasic, Applications of fluorescence spectroscopy in protein conformational changes and intermolecular contacts, BBA Adv. 3 (2023) 100091, https://doi.org/10.1016/j.bbadva.2023.100091.
[46] M. Kaur, M. Bhattacharya, B. Maity, Deciphering conformational changes in human serum albumin induced by bile salts using spectroscopic and molecular modeling approaches, J. Mol. Liq. 390 (2023) 123026, https://doi.org/10.1016/j.molliq.2023.123026.
[47] S. Bhattacharjee, DLS and zeta potential – what they are and what they are not? J. Control. Release 235 (2016) 337–351, https://doi.org/10.1016/j.jconrel.2016.06.017.
[48] F.S. Mohseni-Shahri, M.R. Housaindokht, M.R. Bozorgmehr, A.A. Moosavi-Movahedi, Influence of taxifolin on the human serum albumin–propranolol interaction: multiple spectroscopic and chemometrics investigations and molecular dynamics simulation, J. Solut. Chem. 45 (2016) 265–285, https://doi.org/10.1007/s10953-016-0435-4.
[49] A.B. Gurung, M.A. Ali, J. Lee, M.A. Farah, K.M. Al-Anazi, H. Sami, Molecular modelling studies unveil potential binding sites on human serum albumin for selected experimental and in silico COVID-19 drug candidate molecules, Saudi Journal of Biological Sciences 29 (2022) 53–64, https://doi.org/10.1016/j.sjbs.2021.09.042.
[50] W. Kabsch, C. Sander, Dictionary of protein secondary structure: pattern recognition of hydrogen-bonded and geometrical features, Biopolymers 22 (1983) 2577–2637, https://doi.org/10.1002/bip.360221211.
[51] V. Mishra, R.J. Heath, Structural and biochemical features of human serum albumin essential for eukaryotic cell culture, IJMS 22 (2021) 8411, https://doi.org/10.3390/ijms22168411.
[52] A. Hosainzadeh, M. Gharanfoli, M.R. Saberi, J. Chamani, Probing the interaction of human serum albumin with bilirubin in the presence of aspirin by multi-spectroscopic, molecular modeling and zeta potential techniques: insight on binary and ternary systems, J. Biomol. Struct. Dyn. 29 (2012) 1013–1050, https://doi.org/10.1080/073911012010525029.
[53] R. García-Álvarez, M. Vallet-Regí, Hard and soft protein Corona of nanomaterials: analysis and relevance, Nanomaterials 11 (2021) 888, https://doi.org/10.3390/nano11040888.
[54] W. Liu, J. Rose, S. Plantevin, M. Auffan, J.-Y. Bottero, C. Vidaud, Protein corona formation for nanomaterials and proteins of a similar size: hard or soft corona? Nanoscale 5 (2013) 1658, https://doi.org/10.1039/c2nr33611a.